

UNIVERSIDADE ESTADUAL DE CAMPINAS  
SISTEMA DE BIBLIOTECAS DA UNICAMP  
REPOSITÓRIO DA PRODUÇÃO CIENTÍFICA E INTELLECTUAL DA UNICAMP

**Versão do arquivo anexado / Version of attached file:**

Versão do Editor / Published Version

**Mais informações no site da editora / Further information on publisher's website:**

<https://pubs.acs.org/doi/10.1021/acs.chemmater.1c00081>

**DOI: 10.1021/acs.chemmater.1c00081**

**Direitos autorais / Publisher's copyright statement:**

©2021 by American Chemical Society. All rights reserved.

DIRETORIA DE TRATAMENTO DA INFORMAÇÃO

Cidade Universitária Zeferino Vaz Barão Geraldo

CEP 13083-970 – Campinas SP

Fone: (19) 3521-6493

<http://www.repositorio.unicamp.br>

# Atomically Precise Bottom-Up Synthesis of h-BNC: Graphene Doped with h-BN Nanoclusters

Nataly Herrera-Reinoza,\* Alisson Ceccatto dos Santos, Luis Henrique de Lima, Richard Landers, and Abner de Siervo\*



Cite This: *Chem. Mater.* 2021, 33, 2871–2882



Read Online

ACCESS |



Metrics & More

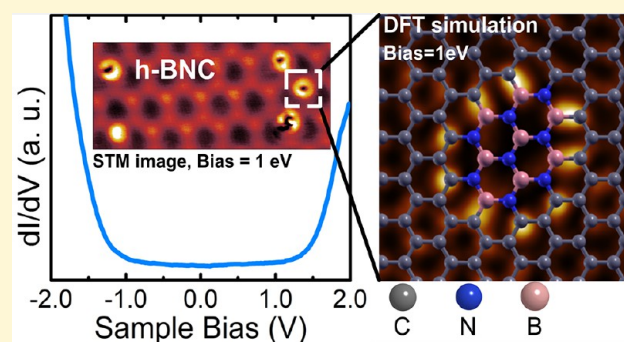


Article Recommendations



Supporting Information

**ABSTRACT:** Monolayer hexagonal boron–nitrogen–carbon (h-BNC) is considered a prominent candidate for the next generation of semiconductor electronic devices. Nevertheless, experimental evidence of h-BNC formation is limited, including a detailed study of its morphological and electronic properties. Here, successful growth of h-BNC from an unexplored single molecular precursor (hexamethyl borazine,  $C_6H_{18}B_3N_3$ ) using a conventional CVD approach on Ir(111) is reported. The conformation structure of the monolayer and its correlation with the local electronic properties are discussed based on scanning tunneling microscopy/spectroscopy (STM/STS) and X-ray photoelectron spectroscopy (XPS) results. The results show an h-BNC structure that can be described as BN-doped graphene since the moiré lattice parameter is preserved along with the alloy. This BN-doped cluster, renamed as h-BN “nanodonuts” according to the electronic density exhibited in STM images, have a tendency to place specific positions within the moiré superstructure, and it is constituted by at least  $(BN)_8$  units arranged in a 6-fold BN rings conformation, as evidenced by simulation of STM images based on density functional theory (DFT). For a BN concentration of about 17%, a band gap between 1.4 and 1.6 eV was determined. The versatility of the novel molecular precursor is proven by the growth of a high-quality h-BN monolayer on Rh(111).



## INTRODUCTION

The growth and characterization of two-dimensional (2D) materials have received tremendous attention in the past decade, since they have exhibited outstanding properties with prominent applications in optoelectronic<sup>1</sup> and quantum transport.<sup>2</sup> Both graphene (Gr) and hexagonal boron nitride (h-BN) have been the most explored 2D materials so far. Even though they show a similar atomic arrangement in an  $sp^2$  honeycomb structure with a lattice mismatch by about 2%,<sup>3,4</sup> they have totally different electronic properties. Graphene is a zero-gap semimetal, which exhibits high carrier mobility<sup>5</sup> and thermal conductivity.<sup>6</sup> The absence of a band gap on the graphene represents the highest barrier to use it in 2D electronic and photonic devices. Unlike graphene, h-BN is an insulating material with a large band gap of 5.9 eV,<sup>7</sup> and the h-BN monolayer has emerged as an ideal template for cluster depositions and spatially confined chemical reactions,<sup>8</sup> can also be applied as a charge leakage barrier-layer in electronic devices,<sup>9,10</sup> and has potential applications in hydrogen storage<sup>11</sup> as well as single photon sources.<sup>12</sup> Based on their morphological and electronic properties, the synthesis of hexagonal monolayers with carbon, boron, and nitrogen atoms within its structure would allow the development of novel materials with a tunable band gap between 0 and ~6 eV, which

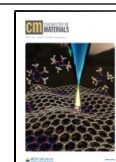
could lead to the growth of innovative 2D semiconductor structures.

Theoretical studies have predicted planar honeycomb feature structures,<sup>13,14</sup> identified as h-BNC alloys formed from building blocks of h-BN and Gr. In systems composed of C, B, and N atoms, it has been found that C–C and B–N bonds tend to be energetically more favorable than other bonds in the system,<sup>13–18</sup> suggesting the segregation of BN units within the graphene lattice, like a substitutional doping, or vice versa, depending on the concentration of each element. Moreover, for h-BNC structures with a given BN doping concentration, it has been reported that the doping-induced band gap can vary over an order of magnitude depending on the sites occupied by the B and N atoms in the network;<sup>19,20</sup> i.e., there is not a monotonic dependence of the band gap with the BN concentration. Due to this predicted semiconductor behavior for ternary h-BNC structures, a plethora of new areas

Received: January 9, 2021

Revised: March 7, 2021

Published: March 24, 2021



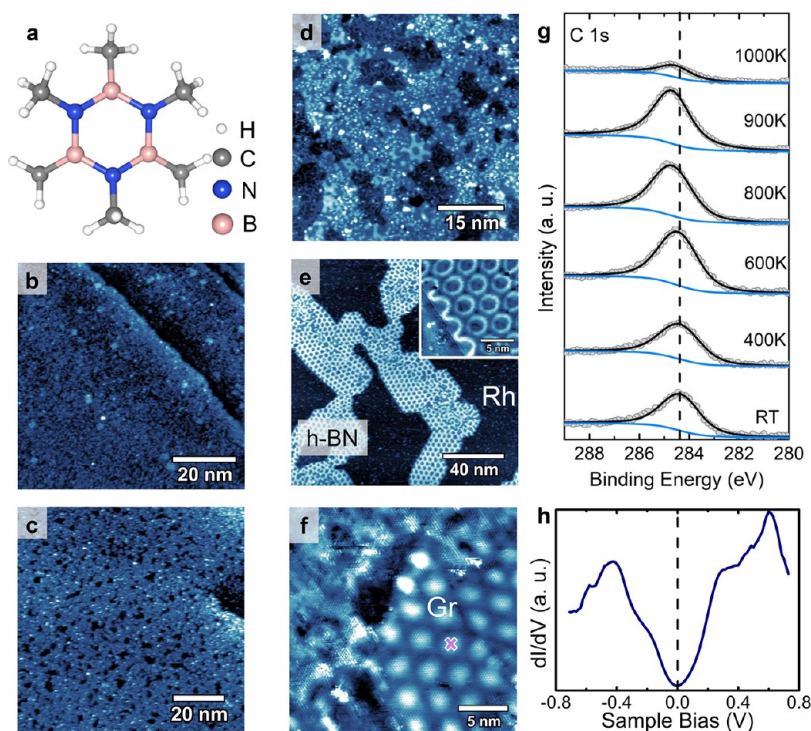


**Figure 1.** On-surface-synthesis process using hexamethyl borazine (HMB) on Rh(111): (a) Sketch of HMB. STM images of the Rh(111) surface after being exposed to molecular precursor at (b) RT, (c) annealing at 800 K, (d) annealing at 900 K, and (e) annealing at 1000 K, where an h-BN autolimited island is observed. The boundary of the island is displayed in the inset image. (f) STM image of a graphene nanoisland formed from precursor deposition with substrate at 800 K and subsequent annealing at 900 K. (g) C 1s core-level XPS spectrum acquired for each thermal treatment carried out on the Rh(111) surface after precursor deposition at RT. The XPS data were collected at a grazing emission angle of  $60^\circ$  from the surface normal. The dashed line indicates the peak position at RT. (h) Representative STS curve acquired on the top of the moiré pattern of the graphene nanoisland shown in part f (position indicated by a cross). Tunneling parameters: (b)  $V = -0.85$  V,  $I_t = -0.73$  nA, (c)  $V = 1.58$  V,  $I_t = 0.12$  nA, (d)  $V = -0.67$  V,  $I_t = -0.30$  nA, (e)  $V = -0.26$  V,  $I_t = -5.30$  nA, and (f)  $V = 0.02$  V,  $I_t = 5.64$  nA.

of applications have emerged, for instance, new potential applications in nanoelectronics<sup>21,22</sup> and nanophotonics devices,<sup>23</sup> photocatalytic activity,<sup>24</sup> gas adsorption,<sup>25</sup> and supercapacitors.<sup>26</sup>

Chemical vapor deposition (CVD) methods have been used to synthesize h-BNC monolayers, and different approaches have been adopted through time. The first report of an h-BNC hybrid structure used two precursor sources introduced at the same time in the preparation chamber, one source for carbon and the other for B and N atoms having as a result random domains of h-BN and Gr, as two segregated phases.<sup>27–29</sup> Measurements of the local density of states (LDOS) by means of scanning tunneling spectroscopy (STS) showed that h-BN domains act as long-range impurities within the graphene lattice inducing a distortion in its zero band gap.<sup>27</sup> Alternatively, lateral h-BN–Gr heterostructures can be obtained by the sequential two-step growth method,<sup>30–32</sup> in which h-BN is grown on preexisting Gr patches (or vice versa). By this method, the domain sizes and the edge structures can be controlled. More recently, with the aim to obtain homogeneous h-BNC structures, several attempts using a single precursor containing C, B, and N atoms in the same molecule have been reported, for instance, dimethylamine borane on Pt(111),<sup>33</sup> trimethylamine borane<sup>34</sup> and methylamine borane<sup>35</sup> on Cu foil, and 1,3,5-trimethylborazine on Co(0001).<sup>36</sup> These studies observed that the h-BN and Gr domains are interconnected forming h-BN–Gr lateral structures. Beniwal et al.<sup>37</sup> reported the synthesis of 2D hexagonal graphenic BNC monolayers using bis-BN cyclo-

hexane on Ir(111); in this case, the grown structure is described as a homogeneous ternary compound of BCN, where the band gap predicted has not been experimentally observed yet. Despite tremendous interest that also includes several theoretical studies,<sup>14,38</sup> experimental evidence of h-BNC formation is limited; in fact, a detailed study of the ternary alloy at the atomic scale and its correlation with the local electronic properties is lacking.

Here, we report the formation of a hexagonal BNC structure as a ternary alloy monolayer obtained from a single molecular precursor, hexamethyl borazine ( $C_6H_{18}B_3N_3$ ) (HMB) shown in Figure 1a. Due to the stoichiometry of this novel precursor, we would expect that the h-BN to Gr ratio should be 1:1 for a totally segregated sample and that, in the case of h-BNC alloy formation, the B:N:C ratio is 1:1:2. Therefore, this is possible considering that the growth happens under conditions that do not benefit a specific  $sp^2$  bond formation (i.e., B–N, C–N, C–B, C–C), leaving the control of the synthesis exclusively to the choice of the substrate conditions. Rh(111) and Ir(111) crystals were chosen as substrates since the on-surface synthesis of Gr and h-BN by CVD has been widely explored on these surfaces. Based on refs 28 and 39–51, we recognized that the growth temperature ranges for Gr and h-BN on Rh(111) and Ir(111) are similar which favors the simultaneous chemical activation of bond breaking and bond formation between the atoms in the precursor. Furthermore, the typical superlattice formed for the h-BN is easily distinguishable from the graphene moiré pattern, which represents an advantage for STM measurements. Thus, this Article aims at providing a

Careful study of h-BNC alloy synthesis using a novel single precursor. We explored in depth its conformation structure and its correlation with local electronic properties by means of scanning tunneling microscopy (STM) and spectroscopy (STS) techniques, including simulated STM images based on density functional theory (DFT), as well as X-ray photoelectron spectroscopy (XPS) to chemically probe the system configuration.

## RESULTS AND DISCUSSION

**Rh(111) Substrate.** In order to explore the adsorption and reaction behavior of HMB as a new precursor to create the so-called  $sp^2$  nanomesh systems with carbon, boron, and nitrogen atoms distributed over the honeycomb lattice, we started with Rh(111) as the substrate. First, the Rh(111) surface was kept at room temperature (RT) while it was exposed to the precursor vapor at  $1.5 \times 10^{-6}$  mbar for 7 min, followed by subsequent annealing treatments. The STM image (see Figure 1b) recorded after the deposition shows the saturation of the surface. The first important conformation changes occur at 800 K, as seen in Figure 1c, given that initial arrangements into the nanoscale cluster are recognized. Figure 1g shows the evolution of the C 1s core level spectrum with temperature. At 800 K the spectrum shows a slight shift of the peak position, which suggests a chemical reaction with new bond formation. At 900 K, carbon atoms are still presented on the surface, and some fragments display the characteristic h-BN nanomesh conformation (see Figure 1d and Figure S1). Self-limited h-BN islands with multiple short domains and a high density of defects are formed after annealing at 1000 K, as displayed in Figure 1e. XPS results also exhibit a considerable decrease in the intensity of the C 1s peak, which indicates that most of the carbon atoms supplied by the precursor are not present on the rhodium surface. Since the last annealing step happened near the temperature where the Rh has a high carbon solubility<sup>52,53</sup> ( $\sim 1100$  K), carbon dissolution into the substrate without the formation of an  $sp^2$  structure at the surface is a rather plausible scenario.

It is important to note that depositing the precursor at RT that saturates the surface with disordered but still intact molecules and subsequently annealing the system does not promote an efficient route to synthesize h-BN, Gr, or h-BNC. A plausible explanation involves the competition between energetic chemical reaction barriers and an efficient on-surface diffusion of the products to overcome the entropy of the disordered system to form an ordered framework. However, the already formed amorphous system with new chemical bonds produced during the annealing treatments is probably blocking an efficient self-assembling, and higher annealing temperatures only decompose the precursor without an appreciable effect on inducing ordering.<sup>40,54,55</sup>

To gain insight on that, additional growths were done with the surface (see Figure S2) previously heated above room temperature. A particularly interesting growth consisted of exposing the Rh(111) surface at 800 K to  $1.4 \times 10^{-6}$  mbar pressure of HMB. The growth under these conditions was chosen, since experimental evidence indicates that the first change in the previous samples happens around this temperature. STM images do not show signs of periodic structure, which makes sense because this temperature is outside of the growth temperature range for both materials (h-BN and Gr) on Rh(111). However, depositing the molecules under this substrate condition could help in understanding the growth

kinetics. For instance, at RT, the precursors and products bind to the surface and have less mobility to form more complex structures. After the deposition at 800 K, we performed an annealing at 900 K, having as a result the formation of small islands, as shown in Figure 1f. These islands are identified as being Gr, corroborated by the following results: (1) We have observed the expected moiré pattern of Gr on Rh(111) with bright protrusions in a dark surrounding (bright-atop contrast) with a periodicity of  $(3.07 \pm 0.07)$  nm, in agreement with the reported values in the literature,<sup>56,57</sup> and (2) the LDOS measured by the STS technique evidences the characteristic V-shape curve of Gr,<sup>58</sup> centered at the Fermi level (0 eV) as can be observed in the STS curve shown in Figure 1h, which was acquired on the top of the moiré pattern. After annealing at 1000 K, the graphene islands disappeared from the surface, and solely h-BN islands are formed (see Figure 2). As described

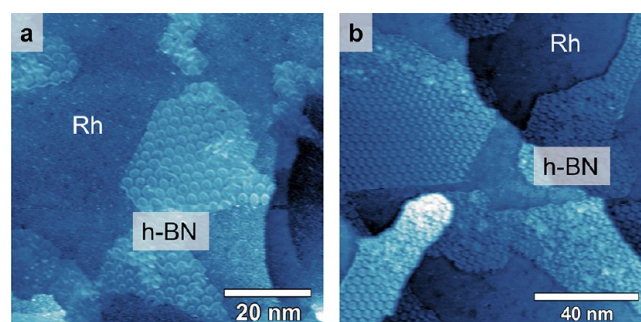


**Figure 2.** On-surface synthesis process using hexamethyl borazine (HMB) on Rh(111): h-BN islands formed on Rh(111) after annealing at 1000 K on the sample kept at 800 K during the precursor deposition process. Tunneling parameters: (a)  $V = -0.01$  V,  $I_t = -0.33$  nA, (b)  $V = -0.01$  V,  $I_t = -5.75$  nA.

above, carbon atoms vanish after thermal annealing at 1000 K; therefore, it is an important point to pay attention in our goal to grow the BNC ternary alloy or hybrid structure of h-BN–Gr from a single precursor on the Rh(111) surface, since the growth temperature of the h-BN coincides with the dissolution temperature of carbon into the Rh bulk. It is worth emphasizing that, under our experimental conditions, it was not possible to observe the graphene dissolve into the rhodium beginning at 1053 K as reported by Dong et al.<sup>40</sup>

Taking these results into account, the high-temperature growth (HTG)<sup>59,60</sup> method was adopted to verify if it is possible to synthesize an h-BN monolayer, similar to what has been done using other precursors without the presence of carbon atoms, for instance, borazine ( $B_3N_3H_6$ ).<sup>39,42</sup> For this purpose, Rh(111) was maintained at 1050 K and exposed to a partial pressure of the precursor of  $1.4 \times 10^{-6}$  mbar for 3 min. In the sequence, the precursor was pumped out while the substrate was kept at the growth temperature for the next 30 min. These growth conditions were chosen based on previous studies<sup>39</sup> that suggest that high temperatures and low flow of borazine favor the formation of large domains of h-BN on Rh(111). The STM images in Figure 3a and Figure S3 show a single h-BN domain crossing the crystal steps as a “carpet”. In addition, the perfect h-BN nanomesh structure free of defects can be observed in detail in Figure 3b. In particular, the inset of Figure 3b displays atomic resolution inside of the so-called “pore region” of the h-BN nanomesh. The nanomesh lattice parameter was found as  $(3.20 \pm 0.03)$  nm, which is a characteristic value of h-BN on Rh(111),<sup>42,61</sup> and corresponds

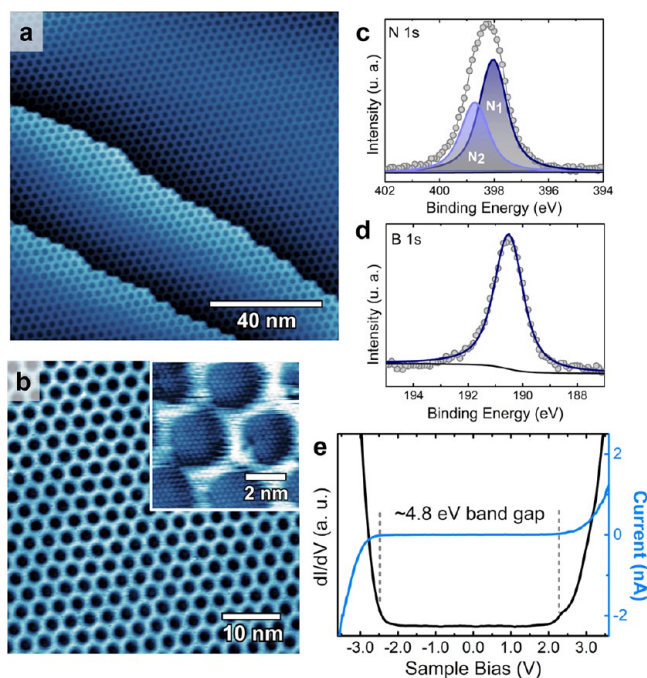


**Figure 3.** h-BN monolayer growth at 1050 K from HMB ( $\text{B}_3\text{N}_3\text{C}_6\text{H}_{18}$ ) on Rh(111): (a) STM large-scale image, where the monolayer continues over several underlying Rh(111) step edges without any visible domain boundaries. (b) STM image of h-BN nanomesh; in the inset, an atomic resolution image of the pore region is displayed. X-ray photoemission spectra of (c) N 1s and (d) B 1s of the h-BN monolayer, acquired at a grazing incidence angle of  $60^\circ$  from the surface normal. The intensity ratio N:B was determined as 1:1. (e) STS (current and differential conductance ( $dI/dV$ )) curves of h-BN show a nonconducting region of  $\sim 4.8$  eV. Tunneling parameters: (a, b)  $V = -0.26$  V,  $I_t = -0.35$  nA, and inset  $V = -0.02$  V,  $I_t = -6.98$  nA.

with  $(13 \times 13)$  unit cells of h-BN on top of  $(12 \times 12)$  unit cells of Rh(111). Figure 3c,d shows XPS spectra for the N 1s and B 1s core level, respectively, obtained after the successful growth of the h-BN monolayer. The intensity ratio N:B was determined as 1:1, which is expected for a perfect h-BN layer. A careful fitting was performed (see Table S1) for N 1s, resulting in the deconvolution of two chemical components  $\text{N}_1$  at  $397.90 \pm 0.05$  eV and  $\text{N}_2$  shifted to higher binding energy  $\sim 0.7$  eV, and an intensity ratio  $\text{N}_1:\text{N}_2$  of 2:1, which agree with other results.<sup>62</sup> These two nitrogen species are associated with the corrugation of h-BN on Rh(111).  $\text{N}_2$  is more strongly bound and corresponds to atoms in the pore region, i.e., aligned with the Rh atoms, and  $\text{N}_1$  refers to atoms aligned with hollow sites (wire region on the nanomesh) and has a weaker interaction with the substrate. Performing STS measurements on this sample, we obtained curves as the one shown in Figure 3e, where a band gap value of about 4.8 eV has been determined by direct comparison of the  $I$ – $V$  and  $dI/dV$  curves.<sup>63–65</sup> This value is in close agreement with previous studies of the electronic properties of h-BN grown on metals like Cu(111)<sup>66,67</sup> and Ir(111),<sup>28</sup> where a band gap around 5.0 eV has been found. The band gap value reported for the h-BN monolayer on HOPG<sup>68</sup> as well as the theoretical prediction for an isolated monolayer is  $\sim 6.0$  eV.<sup>69</sup> h-BN monolayers grown on metallic substrate normally present a band gap reduction, likely due to a strong h-BN–substrate interface interaction.<sup>43</sup>

**Ir(111) Substrate.** Due to the carbon dissolution into the Rh(111) substrate at the typical growth temperature (about 1000 K) of h-BN, this surface is not suitable to form hybrid structures using HMB as a single precursor. Hence, we decided to investigate the on-surface synthesis on the Ir(111) crystal which offers a broader range of growth temperatures for both h-BN and Gr which could also have a huge impact to promote the formation of hybrid materials such as h-BNC alloys. According to previous studies,<sup>41,44–46</sup> Gr usually starts to grow around to 870 K (depending on the source of carbon) and can remain on the surface without notable damage until about 1700 K on Ir(111), making it difficult to form iridium carbide. On the other hand, the higher solubility of boron and desorption of nitrogen atoms as a  $\text{N}_2$  molecule at  $\sim 1400$  K suggest the low stability of h-BN above this temperature and its subsequent decomposition<sup>41,47–49,51</sup> when a molecular precursor like borazine is deposited on Ir(111) at RT. However, for growths performed close to this temperature limit, h-BN islands on Ir(111) have shown a large size with a single orientation.<sup>48,50</sup> The role of the Ir(111) substrate temperature is emphasized in Figure 4, where an illustrative comparison of

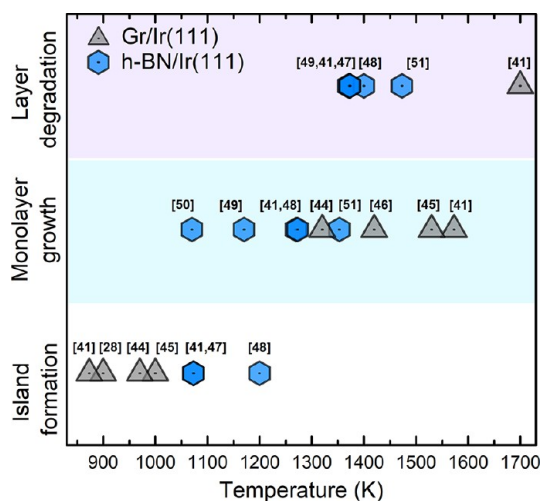


**Figure 4.** Schematic diagram showing the temperature dependence of the island formation, monolayer growth, and thermal degradation of Gr and h-BN on Ir(111) grown using as a precursor ethylene ( $\text{C}_2\text{H}_4$ ) and borazine ( $\text{B}_3\text{N}_3\text{H}_6$ ), respectively.

the stages of island formation, monolayer growth, and thermal degradation of the material is given, for Gr and h-BN growth performed from ethylene and borazine, respectively. Hence, in order to better understand the adsorption and reaction behavior of HMB on Ir(111) and based on the information discussed above, we performed three growth experiments at different synthesis temperatures: 1270, 1370, and 1470 K. Low-temperature syntheses were not considered, since a similar behavior to that exhibited on the Rh(111) surface was expected.

Figure 5a shows a general picture of the sample synthesized at 1470 K. It is possible to distinguish unequivocally the coexistence of three areas with different materials. At the top of the image, we recognize the characteristic feature of the h-BN on Ir(111), with some nanoislands embedded within the h-BN moiré pattern highlighted in yellow; even though these bright structures cannot be atomically resolved in the image, they exhibit clearly a distinct LDOS, presumably due to carbon atoms, i.e., graphene nanoislands. At the bottom-right of Figure

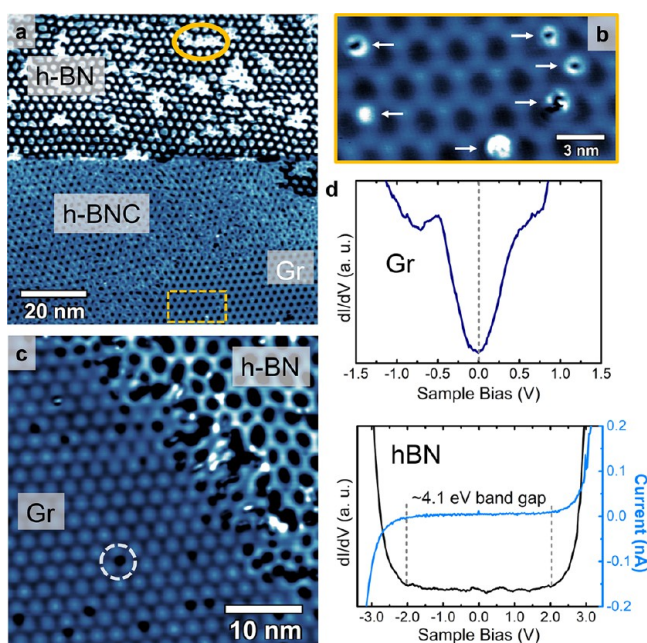


**Figure 5.** Hybrid structure growth from a single novel precursor HMB on Ir(111). (a) STM image of the sample grown at 1470 K evidencing the coexistence of three structures present in the sample, where a nanographene island is pointed out by a yellow circle in the h-BN nanomesh. (b) Zoomed-in STM image of the graphene area indicated by the yellow rectangle in part a, where BN substitutional doping (“BN-nanodonuts”) is indicated by white arrows into the graphene lattice. (c) Boundary region between Gr and h-BN acquired on the sample synthesized at 1370 K. The black dots in the graphene area (white dashed circle) are also BN-nanoclusters. (d) STS curves acquired on the graphene and h-BN. Tunneling parameters: (a, b)  $V = 1.09$  V and  $I_t = 2.75$  nA, (c)  $V = -1.03$  V and  $I_t = -0.31$  nA.

5a, the graphene moiré pattern can be observed, which presents the well-known dark-atop contrast.<sup>70,71</sup> In the zoomed-in image (Figure 5b) of this region (in the yellow rectangle), white arrows indicate the substitutional doping, which are noticed as a brighter ring structure. We propose that these specific features correspond to the presence of BN dopant clusters (“h-BN nanodonut”), since it is expected that B and N atoms tend to form a BN pair in stable Gr:BN structures according to theoretical calculations reported in the literature,<sup>13,14,72–74</sup> where a high energy cost is found to form the C–N and C–B bond as compared to that of B–N bonds. In fact, for systems synthesized under conditions near B:N  $\sim 1$ , it is expected that BN segregates from graphene to form BN regions within the graphene lattice.<sup>15,17</sup> In the center of the image (see Figure 5a), we have a hexagonal mixed region that we have identified as the BNC structure, which can be considered as an alloy of graphene and BN or, in another words, a high density of dopant “h-BN nanodonuts”. A more detailed discussion about their conformation and local electronic properties will be given later.

Figure 5c displays a representative STM image of a lateral heterostructure focusing on the boundary region between Gr and h-BN acquired for the sample grown at 1370 K (see also further details in Figure S4). It is worth noting that both  $sp^2$  structures exhibit an inverse contrast in relation to Figure 5a, allowing us to see the substitutional doping, indicated with a white circle, as dark depressions inside the graphene superlattice. The nature of these superstructures was confirmed

by FT (Fourier transform) calculations of lattice parameter, as well as by STS measurements. For Gr, the superstructure lattice parameter was determined as  $2.47 \pm 0.01$  nm, which is consistent with published results.<sup>44</sup> STS curves were acquired in areas that seem chemically symmetric and where the BN doping is not present or at least located relatively far away ( $\sim 20 \times 20$  nm) from the inspected region. A representative STS curve taken in an atop position on the moiré pattern is shown in Figure 5d, revealing the V-shape characteristic of the Gr density of states symmetric in relation to the Fermi level, indicated by the dotted line. The superstructure periodicity obtained for h-BN was  $2.91 \pm 0.01$  nm, which also corresponds to the reported values in the literature for h-BN on Ir(111).<sup>48,51</sup> The STS result is shown in Figure 5d, where a band gap of about 4.1 eV is obtained. This value is slightly smaller than the one found above for the h-BN on Rh(111), which could be associated with the fact that in this case we did not grow a large h-BN area free of defects. Q. Li and co-workers<sup>66</sup> have demonstrated that some structural defects like grain boundaries can reduce even more the band gap in h-BN monolayers.

In contrast with two samples synthesized at higher temperatures (1470 and 1370 K), the sample obtained at 1270 K did not show large pristine graphene areas; instead, extensive areas of h-BNC are formed, as depicted in a representative STM image in Figure 6a and Figure S5.

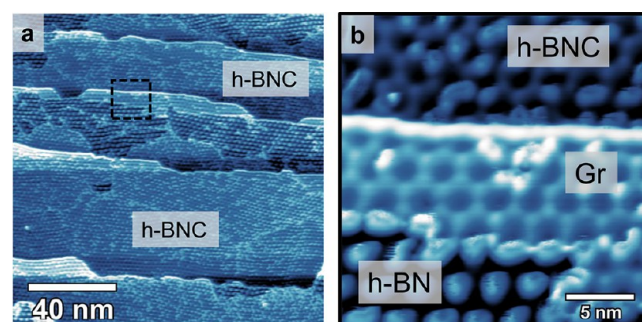


**Figure 6.** (a) Large-scale STM image of the sample grown at 1270 K. (b) Phase-segregated graphene nanoribbon between h-BNC and h-BN. Tunneling parameters: (a, b)  $V = -0.80$  V,  $I_t = -0.20$  nA.

Moreover, one observes some graphene-like regions as phase-segregated ribbons located at the boundary of domains. In the zoomed-in image (Figure 6b), we recognized a strip of graphene, which has a width of  $9.1 \pm 0.8$  nm and can be described as a nanoribbon (GNR) embedded between two different regions, h-BNC and h-BN.

According to these results, the h-BNC structure was observed for all growth conditions performed in this study at different temperatures. However, large domains of the ternary alloy were identified exclusively at 1270 K. Moreover, in this case, the BN substitutional doping, “h-BN nanodonut”, shows a more regular size. In this context, we focused the study of this novel structure on the sample grown at the lowest temperature. Figure 7a displays a large-scan-size STM image of h-BNC. A magnified view of the square-enclosed region is shown in the inset, where an “h-BN nanodonut” is pointed out. The lattice parameter found for the BNC superstructure is  $(2.50 \pm 0.05)$  nm, which indicates that the graphene moiré lattice parameter is preserved along the alloy. A close inspection of STM images reveals that BN doping clusters have a tendency to form in an

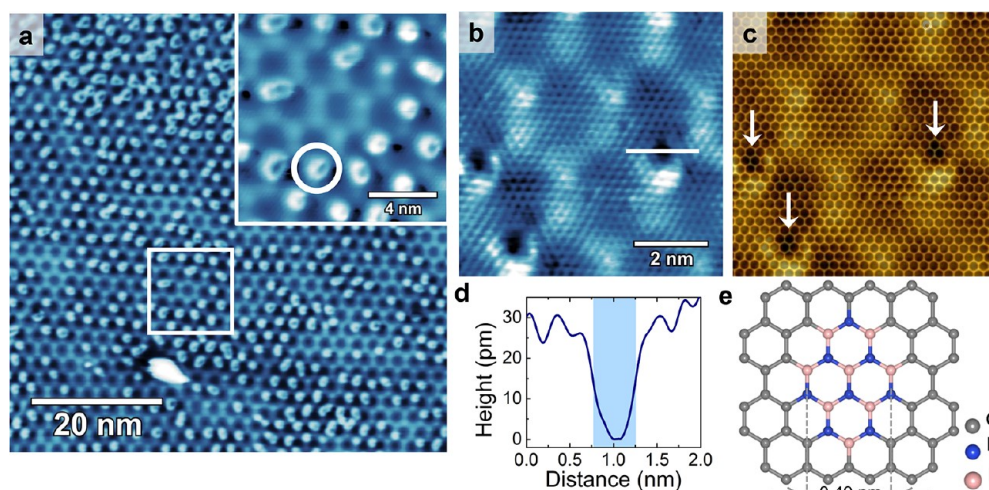


**Figure 7.** h-BNC conformational structure: (a) STM large-scale image, with the inset highlighting the graphene structure doped by the “h-BN nanodonuts”. (b) Atomic resolution image of the h-BNC, where the honeycomb structure of graphene is evident. (c) Superimposed honeycomb graphene structure on the topographic image in part b, white arrows indicating the BN domains. (d) Height profile along the BN cluster in part b, where the shaded area shows the FWHM of the profile. (e) Atomic model of the graphene doped with a small BN cluster. Tunneling parameters: (a and inset)  $V = -1.00$  V,  $I_t = -0.20$  nA, (b)  $V = -0.80$  V,  $I_t = -0.25$  nA.

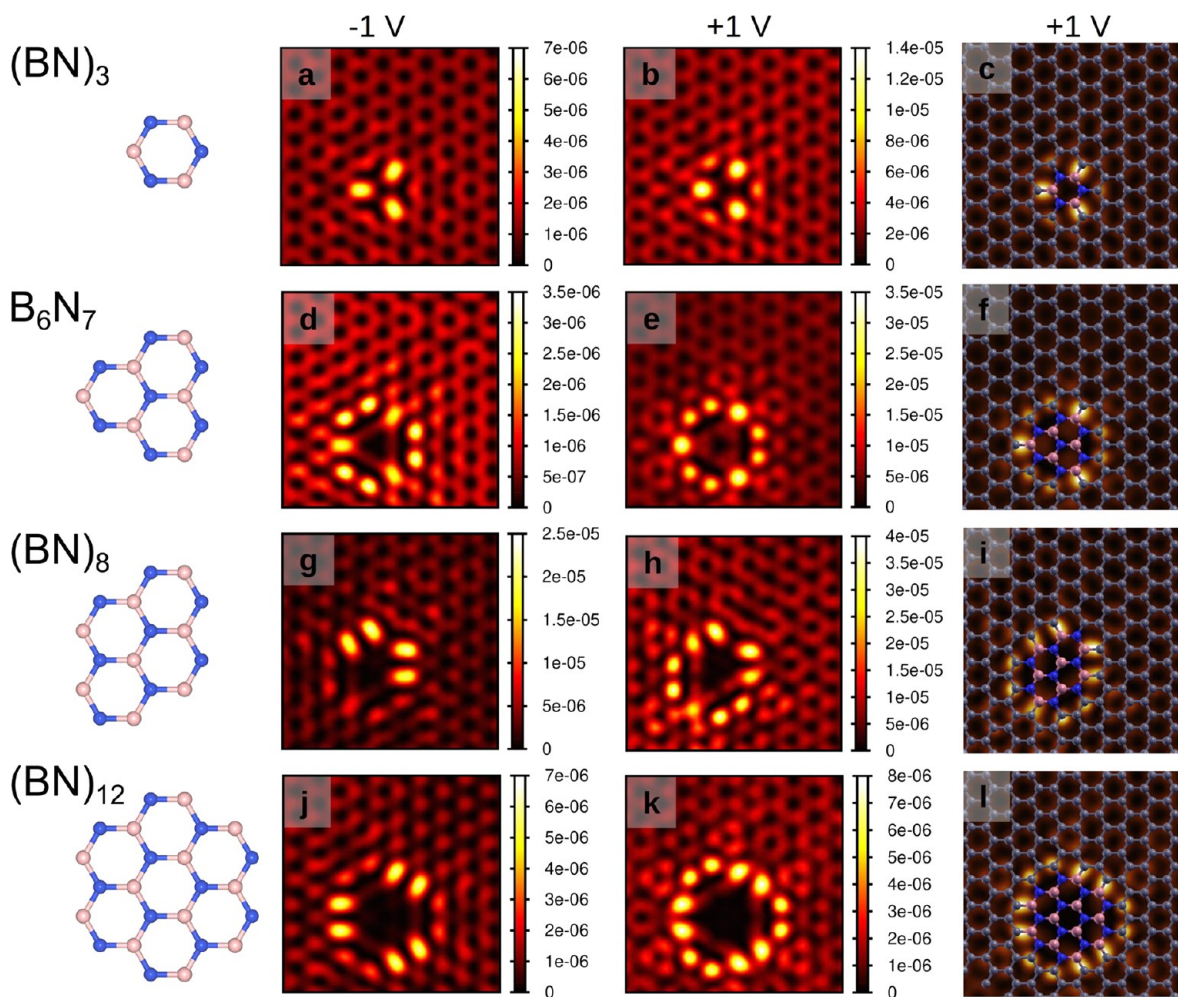


**Figure 8.** Simulated STM images ( $21 \times 21$  Å) representing the electronic density  $\rho_{\text{STM}}$  for clusters of BN embedded in a graphene layer. The left panels are for  $V_{\text{bias}} = -1$  V. The center panels are for  $V_{\text{bias}} = +1$  V. The right panels are for  $V_{\text{bias}} = +1$  V with the structural model superimposed. The coloring of atomic species is as follows: N atoms in blue, B atoms in salmon, and C atoms in gray. The “h-BN nanodonuts” are (a–c)  $(\text{BN})_3$ , (d–f)  $\text{B}_6\text{N}_7$ , (g–i)  $(\text{BN})_8$ , and (j–l)  $(\text{BN})_{12}$ .  $\rho_{\text{STM}}$  is given in units of electrons/a.u.<sup>3</sup>.

hcp-type and fcc-type region on Ir(111),<sup>75</sup> where the interaction of the graphene with the substrate is stronger. The same behavior of the selective doping region can also be identified more clearly (black circular holes) in the other graphene contrast shown in Figure 5c as well as in Figure S6. Balog et al.<sup>76</sup> observed a similar tendency in the hydrogen adsorption on Gr/Ir(111) when this substrate was exposed to atomic hydrogen at a very low dose. In Figure 7b, both the graphene honeycomb lattice and the moiré superstructure are evident. The lattice constant of graphene was determined by FT as  $2.46 \pm 0.06$  Å. Under these specific measurement conditions, the BN clusters are imaged like holes into the lattice. In order to shed light on the atomic structure of the alloy and propose a geometry for the “h-BN nanodons” motifs, we superimposed the honeycomb graphene lattice on the topographic image (Figure 7b) resulting in Figure 7c, where regions associated with the dopant are indicated with white arrows. A height profile along the marked line in Figure 7b is shown in Figure 7d; the full width at half-maximum (fwhm) was found as  $(0.49 \pm 0.07)$  nm, which suggests that the dopant regions are constituted by at least  $(\text{BN})_8$  units arranged as can be seen in Figure 7e. For a low concentration of BN, it is possible that a small amount of BN clusters are substituting in-planar the graphene lattice. A systematic investigation of the STM images demonstrates that these “h-BN nanodons” are extremely regular in shape and size, even if in some regions they appear distorted due to the interconnection of neighbor “h-BN nanodons”. This experimental finding suggests that an optimal size for this nanocluster of BN dopant is obtained during the present synthesis. Ren et al.<sup>74,77</sup> found that 6-fold BN rings are the most favorable structure in BN-doped graphene when compared to other explored motifs like dimers or chains; this is supported by the fact that 6-fold rings of BN are more suitable for  $\pi$  bonding. Fan et al.<sup>78</sup> also calculated the formation energies of BN clusters with different sizes, ranging from a single BN unit to  $(\text{BN})_{12}$ , showing that domains of  $(\text{BN})_{12}$  are energetically more favorable than smaller clusters. Other theoretical studies based on the energetic and structural stability of different motifs in this kind of 2D structures can be found in refs 18 and 79. Therefore, we consider all the theoretical predictions described in the mentioned references to support our interpretation for results in Figure 7, where few BN units (at least 8) are forming clusters inside the Gr lattice. On the other hand, some studies<sup>74,77</sup> have indicated that CVD growth techniques are not suitable for synthesizing non-phase-separated BNC alloys. In fact, they recommend to use deposition techniques such as electron-beam-bombardment. The present work demonstrates that for the particular precursor used an h-BNC alloy can be successfully prepared by the CVD method.

To further support our proposed geometry for the “h-BN nanodons”, we simulated STM images based on density functional theory (DFT) and the Tersoff–Hamann<sup>80,81</sup> approach for height-constant mode. In the simulations presented here, the Ir substrate was not included. Despite the importance of the interaction of graphene with the Ir(111) surface, as observed by the moiré superstructure in the experimental STM images, a weak interaction of graphene with the substrate justifies our approach.<sup>82</sup> Figure 8 shows the simulated STM images. Four “h-BN nanodons” models were tested for  $V_{\text{bias}}$  of  $-1$  and  $+1$  V (sample bias). The BN structures that replace the C atoms in the graphene layer are  $(\text{BN})_3$  (Figure 8a–c),  $\text{B}_6\text{N}_7$  (Figure 8d–f),  $(\text{BN})_8$  (Figure 8g–

i), and  $(\text{BN})_{12}$  (Figure 8j–l). These models were chosen because they are the ones with the shape and size most consistent with the experimental results. The region within the “h-BN nanodons” has a low calculated STM electronic density ( $\rho_{\text{STM}}$ ) for the sample bias investigated. However, for both  $-1$  and  $+1$  V sample bias, there is a high  $\rho_{\text{STM}}$  in the region between the BN cluster and the C atoms, mainly for the B–C bonds, confirming the “donut” structure observed in the experimental images. The structures  $(\text{BN})_3$ ,  $\text{B}_6\text{N}_7$ , and  $(\text{BN})_{12}$  are more circularly symmetrical compared to the elongated shape of  $(\text{BN})_8$ . Moreover, there is an asymmetry in the  $\rho_{\text{STM}}$  for the  $(\text{BN})_8$ , with a high intensity on the side of the BN cluster with more B–C bonds. These features are compatible with the observed experimental results, as clearly seen in Figures 5b and 7b, and corroborate with our proposed model for the “h-BN nanodons” as  $(\text{BN})_8$  clusters embedded in the graphene layer at very specific positions within the moiré superstructure. It is important to stress that such an asymmetric shape in the STM images are not a measurement artifact, since we have confirmed these structures several times and in several samples by changing the scanning directions in the microscope.

To analyze the chemical state of the B, C, and N atoms, the N 1s, B 1s, and C 1s core level XPS spectra obtained for the sample growth at 1270 K are shown in Figure 9a. The

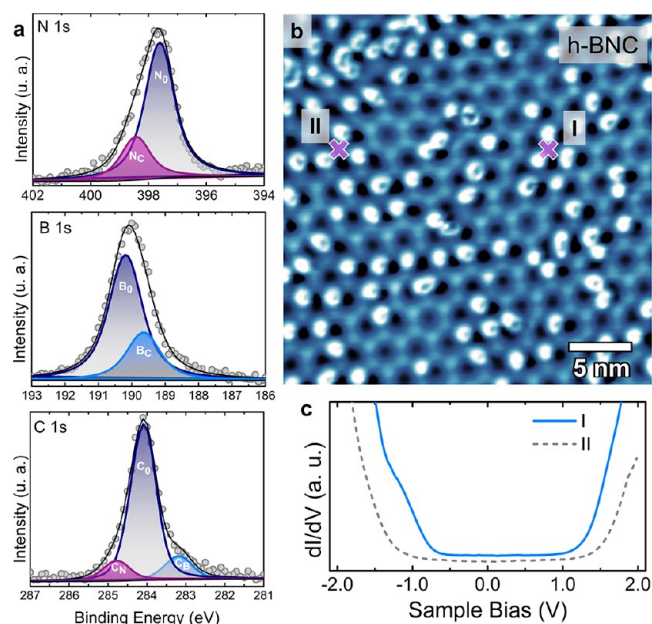


**Figure 9.** (a) N 1s, B 1s, and C 1s X-ray photoemission spectra of the h-BNC monolayer prepared on Ir(111) at 1270 K. XPS spectra were acquired using Mg  $K\alpha$  at a grazing incidence angle of  $60^\circ$  from the surface normal. (b) STM image of h-BNC alloy. (c) STS curves taken on C regions surrounding by doped domains, indicated with the X. Tunneling parameters:  $V = -1.10$  V,  $I_t = -0.24$  nA.

experimental data exhibit a slightly asymmetric peak shape along with large fwhm, which reveals the presence of multiple chemical states in each core level peak. We fitted the raw data using Voigt-like functions in the Lorentzian limit, after subtracting a Shirley-type background. The experimental broadening, related to the Gaussian contribution, has a fwhm fixed to  $\sim 0.6$  eV (which was previously determined). Moreover, the fitting was performed under the constraints of equal fwhm

for the components of the same element (see Table S2). The N 1s core level was fitted with two peaks, a main peak ( $N_0$ ) at  $397.50 \pm 0.05$  eV and second weaker component ( $N_C$ ) at  $398.40 \pm 0.05$  eV. Likewise, a multipoint fitting was performed on the B 1s core level, obtaining the most intense component ( $B_0$ ) at  $190.10 \pm 0.05$  eV and the other one ( $B_C$ ) at  $189.60 \pm 0.05$  eV. The position of the peaks identified as  $N_0$  and  $B_0$  are in excellent agreement with the reported values for h-BN on Ir(111).<sup>28,48</sup> The peak at higher binding energy on N 1s ( $N_C$ ) is assigned to contributions from N–C bonds since C atoms are more electronegative than B, which implies an increase in the binding energy. For B 1s,  $B_C$  is located at a lower binding energy; considering again the electronegativity of C compare with N, this peak is associated with B–C bonds. For the C 1s core level, three peaks can be distinguished. In addition, a similar intensity ratio was found for  $N_C/N_0$  and  $B_C/B_0$  of 8:25 and 19:50, respectively. The dominant component,  $C_0$ , at  $284.00 \pm 0.05$  eV is assigned to  $sp^2$ -hybridized C atoms in pristine graphene on Ir(111).<sup>83,84</sup> The small shoulder at lower binding energy ( $283.10 \pm 0.05$  eV) is attributed to C–B bonds, whereas the other peak at higher binding energy ( $284.70 \pm 0.05$  eV) is assigned to C–N bonds. The chemical analysis above gives support to the formation of h-BNC ternary alloy on the Ir(111) surface, and it is coherent with our proposed structure consisting of a graphene lattice doped with a small cluster of BN, where C–B and C–N bonds are located at the boundaries of the dopant, with a relative concentration between  $C_B$  and  $C_N$  of  $\sim 1:1$ . From XPS data, the formation of h-BN segregated from the alloy is also identified, as observed in the STM images shown in this work. It is clear that a rigorous chemical composition of the alloy is not achievable due to limitations of the XPS measurements, for instance, the low photoemission cross-sections for the core levels explored here, as well as the low-energy resolution provided by the non-monochromatic Mg K $\alpha$  source. Moreover, there is one intrinsic difficulty to separate the BN contribution from h-BN segregated islands from the “h-BN nanodonuts” using XPS. We might overcome this problem by a careful statistical analysis of the BN:C concentration in the h-BNC by counting the BN clusters on the STM images.

Figure 9b shows a representative STM image of the h-BNC region. Based on our analysis and considering one area of  $25 \times 25$  nm<sup>2</sup>, we estimated a BN concentration of about 17%. Since the sample did not grow homogeneously across the crystal, it is not possible to extend this concentration value for the whole sample. In this region, the LDOS by STS was examined, with the spectra displayed in Figure 9c given as more representative examples; these STS curves were acquired around the “h-BN nanodonuts”. It is important to note that the spacial resolution and locality of STS make it one of the most suitable techniques to explore the electronic structure of the h-BNC alloy characterized by a low BN segregation in the graphene lattice located into a highly heterogeneous sample, unlike other techniques such as angle-resolved photoemission spectroscopy (ARPES), which has been the most employed tool to investigate the band gap opening in graphene and given a global measurement of the band structure.<sup>85</sup> Otherwise, as predicted by theoretical calculations, the introduction of BN domains in the carbon lattice breaks the potential symmetry leading to the redistribution of charge near the Dirac points and the band gap opening. For the area shown in Figure 9b, we have estimated a band gap between 1.4 and 1.6 eV, curve I and II, respectively. Despite this, band gap values for h-BNC

structures determined by computational models depend on both the stoichiometry of the alloy and the concentration of BN and carbon atoms; our result is consistent with predictions<sup>15,78</sup> made for some  $BN_xC_{(1-x)}$  materials. In addition, these values are inside the band gap range determined for similar samples by means of optical spectroscopy.<sup>86,87</sup> However, a careful study of the band gap opening and the determination of the band gap value for this structure is desired in further investigations, for instance, employing low-temperature STS or nano-ARPES measurements.<sup>88,89</sup>

## CONCLUSION

In this work, we have used the unexplored precursor hexamethyl borazine (HMB) to successfully grown epitaxial h-BN, hybrid lateral junctions of h-BN and graphene, as well as the h-BNC alloys on Ir(111) by using conventional CVD methods. The combination of substrate and the correct temperature window plays an important role on growing h-BNC. On one hand, graphene can be efficiently grown on Rh(111) at low temperatures ( $\sim 900$  K), while h-BN is formed only above 1000 K. However, at such high temperatures, C strongly dissolves into the Rh bulk; thus, the coexistence of h-BN and graphene is very difficult in such a substrate, with only a perfect h-BN monolayer remaining on Rh(111). On the other hand, C has a very low dissolution into Ir(111), and graphene is efficiently formed at much higher temperatures (above 1200 K) being very stable until temperatures like 1700 K. Similarly, h-BN starts to efficiently grow on Ir(111) at temperatures like 1100 K and remains stable up to temperatures  $\sim 1400$  K. Therefore, we have a large growth window to produce h-BN and graphene as well as induce the h-BNC alloy formation in the interval of 1200–1500 K, where lower temperatures will promote h-BN and higher temperatures graphene. For all ranges of temperatures investigated in the present work, we found the formation of h-BNC on Ir(111). Using atomic resolution STM images combined with DFT calculation, we have demonstrated that h-BNC is formed by doping graphene with small BN nanoclusters. Theoretical predictions by Fan et al.<sup>78</sup> suggested that  $(BN)_{12}$  clusters are energetically favored. The atomic resolved STM images revealed a predominance of an asymmetric density in the image contrast around the BN nanoclusters (BN “nanodonuts”) that DFT calculations associate with  $(BN)_8$ . Moreover, the BN-nanocluster is preferentially formed only in the fcc- and hcp-type regions of the graphene moiré pattern on Ir(111) as defined by N'Diaye et al.<sup>75</sup> Therefore, we might speculate that such preferential “formation sites” would limit the density of the BN-cluster on graphene, leading to extra control on the band gap value, which might be optimized on fine-tuning of the growth conditions and substrate, for instance, on Ir alloys.

## MATERIALS AND METHODS

**CVD, XPS, and STM Experiments.** The hexamethyl borazine (HMB) molecule (Sigma-Aldrich) was preserved from light and maintained at  $\sim 253$  K to avoid its degradation due to photothermal decomposition. To perform the growths, the molecules in powder form were introduced into a quartz ampule which was also kept below  $\sim 253$  K inside a Peltier cooler. The reservoir was connected to the UHV chamber via a leak valve. It is also connected to a valve that allows differential pumping down to  $10^{-4}$  mbar. Prior to the growth experiments, the precursor was purified by heating and pumping cycles. To introduce HMB into the UHV chamber, it was heated at 350 K, where the entire molecule (164.7 g/mol) was detected by the mass spectrometer (see Figure S7 in the Supporting Information),

which suggests that HMB precursor did not degrade during evaporation. The Rh(111) and Ir(111) substrate were cleaned by successive cycles of energetic (1000 V) Ar<sup>+</sup> ion sputtering and subsequent annealing at 1420 and 1470 K, respectively. For the STM/STS measurement, a SPECS Aarhus 150 instrument was used with a tungsten tip cleaned *in situ* by Ar<sup>+</sup> sputtering and equipped with a SPECS SPC 260 controller. All STM data were acquired at RT, with a base pressure of  $6 \times 10^{-11}$  mbar and in the constant current mode where bias is applied to the sample while the tip is maintained closed to ground potential. The images were analyzed using WSxM<sup>90</sup> and Gwyddion<sup>91</sup> software. The preparation and XPS chamber has a base pressure of  $2 \times 10^{-10}$  mbar. XPS spectra were obtained using a Mg K $\alpha$  source with a photon energy of 1253.6 eV and the SPECS PHOIBOS 150 hemispherical analyzer with multichanneltron detection. These spectra were fitted with a Lorentzian line shape characterized by a full width half-maximum  $\Gamma$ , which takes into account the finite core-hole lifetime plus X-ray contribution. We have used Lorentzian doublets with peaks separated by  $\sim 0.3$  eV and relative intensity of 0.5 to take into account the K $\alpha_{1,2}$  contributions. All peaks were convoluted to a Gaussian distribution (fixed width) that describes the instrumental broadening, phonon contributions, and sample inhomogeneities. The inelastic background contribution was removed using the Shirley type background.

**DFT Simulations.** DFT computations were performed using the Quantum ESPRESSO package<sup>92</sup> within the projector-augmented wave method (PAW).<sup>93</sup> The generalized gradient approximation (GGA) expressed by the PBE functional<sup>94</sup> and a 503 eV cutoff for the plane-wave basis set were adopted. The Brillouin zone was sampled with an  $8 \times 8 \times 1$  centered  $k$  points grid. The sp<sup>2</sup> monolayers were modeled by a periodic  $10 \times 10$  (200 atoms) slab geometry with a vacuum thickness of 12 Å. The lattice parameters were established with the consideration of Vegard's law<sup>78</sup> using the optimized lattice parameters of graphene ( $a_G = 2.469$  Å) and h-BN ( $a_{BN} = 2.516$  Å). Simulated STM images, representing the electronic density  $\rho_{STM}(\mathbf{r}, V_{bias})$  at various bias voltages  $V_{bias}$ , were obtained in the Tersoff–Hamann approximation.<sup>80,81</sup> The STM images were simulated for the height-constant mode with a tip–surface distance of 1.2 Å.

## ■ ASSOCIATED CONTENT

### SI Supporting Information

The Supporting Information is available free of charge at <https://pubs.acs.org/doi/10.1021/acs.chemmater.1c00081>.

STM images of the h-BN synthesis process on Rh(111); XPS analysis details of h-BN/Rh(111) and h-BNC/Ir(111); additional STM images of the coexistence between h-BN, h-BNC, and Gr for growth performed at 1270 and 1370 K on Ir(111); and the molecular precursor mass spectrum (PDF)

## ■ AUTHOR INFORMATION

### Corresponding Authors

Nataly Herrera-Reinoza – Institute of Physics “Gleb Wataghin”, State University of Campinas, 13083-859 Campinas, Brazil; [orcid.org/0000-0001-5658-9692](https://orcid.org/0000-0001-5658-9692); Email: [nherrera@ifi.unicamp.br](mailto:nherrera@ifi.unicamp.br)

Abner de Siervo – Institute of Physics “Gleb Wataghin”, State University of Campinas, 13083-859 Campinas, Brazil; [orcid.org/0000-0002-7192-4740](https://orcid.org/0000-0002-7192-4740); Email: [asiervo@ifi.unicamp.br](mailto:asiervo@ifi.unicamp.br)

### Authors

Alisson Ceccatto dos Santos – Institute of Physics “Gleb Wataghin”, State University of Campinas, 13083-859 Campinas, Brazil; [orcid.org/0000-0001-7619-3062](https://orcid.org/0000-0001-7619-3062)

Luis Henrique de Lima – Centro de Ciências Naturais e Humanas, Federal University of ABC, 09210-580 Santo André, Brazil; [orcid.org/0000-0001-8432-2637](https://orcid.org/0000-0001-8432-2637)

Richard Landers – Institute of Physics “Gleb Wataghin”, State University of Campinas, 13083-859 Campinas, Brazil; [orcid.org/0000-0001-9205-1822](https://orcid.org/0000-0001-9205-1822)

Complete contact information is available at: <https://pubs.acs.org/doi/10.1021/acs.chemmater.1c00081>

## Author Contributions

N.H.R., A.C.d.S., and A.d.S. performed the STM and XPS measurements at Instituto de Física Gleb Wataghin in Campinas, Brazil. L.H.d.L. performed the DFT calculations. N.H.R. analyzed the data. N.H.R., L.H.d.L., and A.d.S. cowrote the paper. A.d.S. conceived the study. R.L. and A.d.S. provided funding acquisition. All authors have read and given approval to the final version of the manuscript.

## Notes

The authors declare no competing financial interest.

## ■ ACKNOWLEDGMENTS

The author are thankful for the financial support from Fundação de Amparo à Pesquisa do Estado de São Paulo (FAPESP) under the project numbers 2007/08244-5, 2007/54829-5, and 2017/18574-4 and from Conselho Nacional Científico e Tecnológico (CNPq) under the project numbers 424633/2018-3 and 304119/2019-9. N.H.R. thanks CNPq for the studentship support. L.H.d.L. thanks FAPESP for the studentship support under project number 2016/21402-8.

## ■ REFERENCES

- (1) Mak, K. F.; Lee, C.; Hone, J.; Shan, J.; Heinz, T. F. Atomically Thin MoS<sub>2</sub>: A New Direct-Gap Semiconductor. *Phys. Rev. Lett.* **2010**, *105*, 136805.
- (2) Liu, X.; Hersam, M. C. 2D materials for quantum information science. *Nature Reviews Materials* **2019**, *4*, 669–684.
- (3) Cooper, D. R.; D'Anjou, B.; Ghattamaneni, N.; Harack, B.; Hilke, M.; Horth, A.; Majlis, N.; Massicotte, M.; Vandsburger, L.; Whiteway, E.; Yu, V. Experimental Review of Graphene. *ISRN Condensed Matter Physics* **2012**, *2012*, 501686.
- (4) Lynch, R. W.; Drickamer, H. G. Effect of High Pressure on the Lattice Parameters of Diamond, Graphite, and Hexagonal Boron Nitride. *J. Chem. Phys.* **1966**, *44*, 181–184.
- (5) Bolotin, K. I.; Sikes, K. J.; Hone, J.; Stormer, H. L.; Kim, P. Temperature-Dependent Transport in Suspended Graphene. *Phys. Rev. Lett.* **2008**, *101*, 096802.
- (6) Balandin, A. A.; Ghosh, S.; Bao, W.; Calizo, I.; Teweldebrhan, D.; Miao, F.; Lau, C. N. Superior Thermal Conductivity of Single-Layer Graphene. *Nano Lett.* **2008**, *8*, 902–907.
- (7) Kubota, Y.; Watanabe, K.; Tsuda, O.; Taniguchi, T. Deep Ultraviolet Light-Emitting Hexagonal Boron Nitride Synthesized at Atmospheric Pressure. *Science* **2007**, *317*, 932–934.
- (8) Auwärter, W. Hexagonal boron nitride monolayers on metal supports: Versatile templates for atoms, molecules and nanostructures. *Surf. Sci. Rep.* **2019**, *74*, 1–95.
- (9) Zhang, K.; Feng, Y.; Wang, F.; Yang, Z.; Wang, J. Two dimensional hexagonal boron nitride (2D-hBN): synthesis, properties and applications. *J. Mater. Chem. C* **2017**, *5*, 11992–12022.
- (10) Siškings, M.; Mullan, C.; Son, S.-K.; Yin, J.; Watanabe, K.; Taniguchi, T.; Ghazaryan, D.; Novoselov, K. S.; Mishchenko, A. High-temperature electronic devices enabled by hBN-encapsulated graphene. *Appl. Phys. Lett.* **2019**, *114*, 123104.
- (11) Chen, X.; Gao, X. P.; Zhang, H.; Zhou, Z.; Hu, W. K.; Pan, G. L.; Zhu, H. Y.; Yan, T. Y.; Song, D. Y. Preparation and

Electrochemical Hydrogen Storage of Boron Nitride Nanotubes. *J. Phys. Chem. B* **2005**, *109*, 11525–11529.

(12) Vogl, T.; Lecomwasam, R.; Buchler, B. C.; Lu, Y.; Lam, P. K. Compact Cavity-Enhanced Single-Photon Generation with Hexagonal Boron Nitride. *ACS Photonics* **2019**, *6*, 1955–1962.

(13) Zhang, M.; Gao, G.; Kutana, A.; Wang, Y.; Zou, X.; Tse, J. S.; Yakobson, B. I.; Li, H.; Liu, H.; Ma, Y. Two-dimensional boron-nitrogen-carbon monolayers with tunable direct band gaps. *Nanoscale* **2015**, *7*, 12023–12029.

(14) Jamróz, A.; Majewski, J. A. Morphology, Ordering, Stability, and Electronic Structure of Carbon-Doped Hexagonal Boron Nitride. *Phys. Status Solidi B* **2019**, *256*, 1800554.

(15) Guilhon, I.; Marques, M.; Teles, L. K.; Bechstedt, F. Optical absorbance and band-gap engineering of  $(\text{BN})_{1-x}(\text{C}_2)_x$  two-dimensional alloys: Phase separation and composition fluctuation effects. *Phys. Rev. B: Condens. Matter Mater. Phys.* **2017**, *95*, 035407.

(16) D'Souza, R.; Mukherjee, S.; Saha-Dasgupta, T. Influence of interface geometry on phase stability and bandgap engineering in boron nitride substituted graphene: A combined first-principles and Monte Carlo study. *J. Alloys Compd.* **2017**, *708*, 437–443.

(17) da Rocha Martins, J.; Chacham, H. Disorder and Segregation in B-C-N Graphene-Type Layers and Nanotubes: Tuning the Band Gap. *ACS Nano* **2011**, *5*, 385–393.

(18) Azevedo, S. Energetic and electronic structure of BC<sub>2</sub>N compounds. *Eur. Phys. J. B* **2005**, *44*, 203–207.

(19) Zhao, R.; Wang, J.; Yang, M.; Liu, Z.; Liu, Z. BN-Embedded Graphene with a Ubiquitous Gap Opening. *J. Phys. Chem. C* **2012**, *116*, 21098–21103.

(20) Nascimento, R.; Martins, J. d. R.; Batista, R. J. C.; Chacham, H. Band Gaps of BN-Doped Graphene: Fluctuations, Trends, and Bounds. *J. Phys. Chem. C* **2015**, *119*, S055–S061.

(21) Uddin, M. R.; Li, J.; Lin, J. Y.; Jiang, H. X. Carbon-rich hexagonal (BN)C alloys. *J. Appl. Phys.* **2015**, *117*, 215703.

(22) Fiori, G.; Betti, A.; Bruzzone, S.; Iannaccone, G. Lateral Graphene-hBCN Heterostructures as a Platform for Fully Two-Dimensional Transistors. *ACS Nano* **2012**, *6*, 2642–2648.

(23) Alcaraz Iranzo, D.; Nanot, S.; Dias, E. J. C.; Epstein, I.; Peng, C.; Efetov, D. K.; Lundberg, M. B.; Parret, R.; Osmond, J.; Hong, J.-Y.; Kong, J.; Englund, D. R.; Peres, N. M. R.; Koppens, F. H. L. Probing the ultimate plasmon confinement limits with a van der Waals heterostructure. *Science* **2018**, *360*, 291–295.

(24) Li, M.; Wang, Y.; Tang, P.; Xie, N.; Zhao, Y.; Liu, X.; Hu, G.; Xie, J.; Zhao, Y.; Tang, J.; Zhang, T.; Ma, D. Graphene with Atomic-Level In-Plane Decoration of h-BN Domains for Efficient Photocatalysis. *Chem. Mater.* **2017**, *29*, 2769–2776.

(25) Chen, S.; Li, P.; Xu, S.; Pan, X.; Fu, Q.; Bao, X. Carbon doping of hexagonal boron nitride porous materials toward CO<sub>2</sub> capture. *J. Mater. Chem. A* **2018**, *6*, 1832–1839.

(26) Wang, S.; Ma, F.; Jiang, H.; Shao, Y.; Wu, Y.; Hao, X. Band gap-Tunable Porous Borocarbonitride Nanosheets for High Energy-Density Supercapacitors. *ACS Appl. Mater. Interfaces* **2018**, *10*, 19588–19597.

(27) Ci, L.; Song, L.; Jin, C.; Jariwala, D.; Wu, D.; Li, Y.; Srivastava, A.; Wang, Z. F.; Storr, K.; Balicas, L.; Lui, F.; Ajayan, P. M. Atomic layers of hybridized boron nitride and graphene domains. *Nat. Mater.* **2010**, *9*, 430–435.

(28) Liu, M.; Li, Y.; Chen, P.; Sun, J.; Ma, D.; Li, Q.; Gao, T.; Gao, Y.; Cheng, Z.; Qiu, X.; Fang, Y.; Zhang, Y.; Liu, Z. Quasi-Freestanding Monolayer Heterostructure of Graphene and Hexagonal Boron Nitride on Ir(111) with a Zigzag Boundary. *Nano Lett.* **2014**, *14*, 6342–6347.

(29) Chang, C.-K.; et al. Band Gap Engineering of Chemical Vapor Deposited Graphene by in Situ BN Doping. *ACS Nano* **2013**, *7*, 1333–1341.

(30) Gao, Y.; Zhang, Y.; Chen, P.; Li, Y.; Liu, M.; Gao, T.; Ma, D.; Chen, Y.; Cheng, Z.; Qiu, X.; Duan, W.; Liu, Z. Toward Single-Layer Uniform Hexagonal Boron Nitride-Graphene Patchworks with Zigzag Linking Edges. *Nano Lett.* **2013**, *13*, 3439–3443.

(31) Lu, J.; Zhang, K.; Feng, L.; X.; Zhang, H.; Sum, T.; Castro Neto, A. H.; Ping, Loh, K. Order-disorder transition in a two-dimensional boron-carbon-nitride alloy. *Nat. Commun.* **2013**, *4*, 2681.

(32) Gong, Y.; et al. Direct chemical conversion of graphene to boron- and nitrogen- and carbon-containing atomic layers. *Nat. Commun.* **2014**, *5*, 3193.

(33) Nappini, S.; Piš, I.; Mentes, T. O.; Sala, A.; Cattelan, M.; Agnoli, S.; Bondino, F.; Magnano, E. Formation of a Quasi-Free-Standing Single Layer of Graphene and Hexagonal Boron Nitride on Pt(111) by a Single Molecular Precursor. *Adv. Funct. Mater.* **2016**, *26*, 1120–1126.

(34) Tay, R. Y.; Li, H.; Tsang, S. H.; Zhu, M.; Loeblein, M.; Jing, L.; Leong, F. N.; Teo, E. H. T. Trimethylamine Borane: A New Single-Source Precursor for Monolayer h-BN Single Crystals and h-BCN Thin Films. *Chem. Mater.* **2016**, *28*, 2180–2190.

(35) Leardini, F.; et al. Chemical vapor deposition growth of boron-carbon-nitrogen layers from methylamine borane thermolysis products. *Nanotechnology* **2018**, *29*, 025603.

(36) Bokai, K. A.; Tarasov, A. V.; Shevlev, V. O.; Vilkov, O. Y.; Makarova, A. A.; Marchenko, D.; Petukhov, A. E.; Muntwiler, M.; Fedorov, A. V.; Voroshnin, V. Y.; Yashina, L. V.; Laubschat, C.; Vyalikh, D. V.; Usachov, D. Y. Hybrid h-BN-Graphene Monolayer with B-C Boundaries on a Lattice-Matched Surface. *Chem. Mater.* **2020**, *32*, 1172–1181.

(37) Beniwal, S.; Hooper, J.; Miller, D. P.; Costa, P. S.; Chen, G.; Liu, S.-Y.; Dowben, P. A.; Sykes, E. C. H.; Zurek, E.; Enders, A. Graphene-like Boron-Carbon-Nitrogen Monolayers. *ACS Nano* **2017**, *11*, 2486–2493.

(38) Jamróz, A.; Majewski, J. A. Ordering effects in 2D hexagonal systems of binary and ternary C-B-N alloys. *Comput. Mater. Sci.* **2018**, *147*, 115–123.

(39) Dong, G.; Fourré, E. B.; Tabak, F. C.; Frenken, J. W. M. How Boron Nitride Forms a Regular Nanomesh on Rh(111). *Phys. Rev. Lett.* **2010**, *104*, 096102.

(40) Dong, G. C.; van Baarle, D. W.; Rost, M. J.; Frenken, J. W. M. Graphene formation on metal surfaces investigated by in-situ scanning tunneling microscopy. *New J. Phys.* **2012**, *14*, 053033.

(41) Usachov, D.; Fedorov, A.; Vilkov, O.; Adamchuk, V. K.; Yashina, L. V.; Bondarenko, L.; Saranin, A. A.; Grüneis, A.; Vyalikh, D. V. Experimental and computational insight into the properties of the lattice-mismatched structures: Monolayers of h-BN and graphene on Ir(111). *Phys. Rev. B: Condens. Matter Mater. Phys.* **2012**, *86*, 155151.

(42) Corso, M.; Auwärter, W.; Muntwiler, M.; Tamai, A.; Greber, T.; Osterwalder, J. Boron Nitride Nanomesh. *Science* **2004**, *303*, 217–220.

(43) Qi, Y.; Han, N.; Li, Y.; Zhang, Z.; Zhou, X.; Deng, B.; Li, Q.; Liu, M.; Zhao, J.; Liu, Z.; Zhang, Y. Strong Adlayer-Substrate Interactions “Break” the Patching Growth of h-BN onto Graphene on Re(0001). *ACS Nano* **2017**, *11*, 1807–1815.

(44) N'Diaye, A. T.; Coraux, J.; Plasa, T. N.; Busse, C.; Michely, T. Structure of epitaxial graphene on Ir(111). *New J. Phys.* **2008**, *10*, 043033.

(45) Hattab, H.; N'Diaye, A. T.; Wall, D.; Jnawali, G.; Coraux, J.; Busse, C.; van Gastel, R.; Poelsema, B.; Michely, T.; Meyer zu Heringdorf, F.-J.; Horn-von Hoegen, M. Growth temperature dependent graphene alignment on Ir(111). *Appl. Phys. Lett.* **2011**, *98*, 141903.

(46) Busse, C.; Lazić, P.; Djemour, R.; Coraux, J.; Gerber, T.; Atodiresei, N.; Caciuc, V.; Brako, R.; N'Diaye, A. T.; Blügel, S.; Zegenhagen, J.; Michely, T. Graphene on Ir(111): Physisorption with Chemical Modulation. *Phys. Rev. Lett.* **2011**, *107*, 036101.

(47) Petrović, M.; Hagemann, U.; Horn-von Hoegen, M.; Meyer zu Heringdorf, F.-J. Microanalysis of single-layer hexagonal boron nitride islands on Ir(111). *Appl. Surf. Sci.* **2017**, *420*, 504–510.

(48) Farwick zum Hagen, F. H.; et al. Structure and Growth of Hexagonal Boron Nitride on Ir(111). *ACS Nano* **2016**, *10*, 11012–11026.

- (49) Orlando, F.; Larciprete, R.; Lacovig, P.; Boscarato, I.; Baraldi, A.; Lizzit, S. Epitaxial Growth of Hexagonal Boron Nitride on Ir(111). *J. Phys. Chem. C* **2012**, *116*, 157–164.
- (50) Orlando, F.; Lacovig, P.; Omiciuolo, L.; Apostol, N. G.; Larciprete, R.; Baraldi, A.; Lizzit, S. Epitaxial Growth of a Single-Domain Hexagonal Boron Nitride Monolayer. *ACS Nano* **2014**, *8*, 12063–12070.
- (51) Schulz, F.; Drost, R.; Hämäläinen, S. K.; Demonchaux, T.; Seitsonen, A. P.; Liljeroth, P. Epitaxial hexagonal boron nitride on Ir(111): A work function template. *Phys. Rev. B: Condens. Matter Mater. Phys.* **2014**, *89*, 235429.
- (52) Arnoult, W. J.; McLellan, R. B. The solubility of carbon in rhodium ruthenium, iridium and rhenium. *Scr. Metall.* **1972**, *6*, 1013–1018.
- (53) Liu, M.; Gao, Y.; Zhang, Y.; Zhang, Y.; Ma, D.; Ji, Q.; Gao, T.; Chen, Y.; Liu, Z. Single and Polycrystalline Graphene on Rh(111) Following Different Growth Mechanisms. *Small* **2013**, *9*, 1360–1366.
- (54) Celis, A.; Nair, M. N.; Sicot, M.; Nicolas, F.; Kubsy, S.; Taleb-Ibrahimi, A.; Malterre, D.; Tejeda, A. Growth, morphology and electronic properties of epitaxial graphene on vicinal Ir(332) surface. *Nanotechnology* **2020**, *31*, 285601.
- (55) Günther, S.; Dänhardt, S.; Ehrensperger, M.; Zeller, P.; Schmitt, S.; Wintterlin, J. High-Temperature Scanning Tunneling Microscopy Study of the Ordering Transition of an Amorphous Carbon Layer into Graphene on Ruthenium(0001). *ACS Nano* **2013**, *7*, 154–164.
- (56) Sicot, M.; Bouvron, S.; Zander, O.; Rüdiger, U.; Dedkov, Y.; Fonin, M. Nucleation and growth of nickel nanoclusters on graphene Moire on Rh(111). *Appl. Phys. Lett.* **2010**, *96*, 093115.
- (57) Voloshina, E. N.; Dedkov, Y. S.; Torbrügge, S.; Thissen, A.; Fonin, M. Graphene on Rh(111): Scanning tunneling and atomic force microscopy studies. *Appl. Phys. Lett.* **2012**, *100*, 241606.
- (58) Yang, M.; Liu, Y.; Fan, T.; Zhang, D. Metal-graphene interfaces in epitaxial and bulk systems: A review. *Prog. Mater. Sci.* **2020**, *110*, 100652.
- (59) Kordina, O.; Hallin, C.; Ellison, A.; Bakin, A. S.; Ivanov, I. G.; Henry, A.; Yakimova, R.; Touminen, M.; Vehanen, A.; Janzén, E. High temperature chemical vapor deposition of SiC. *Appl. Phys. Lett.* **1996**, *69*, 1456–1458.
- (60) Ellison, A.; Zhang, J.; Peterson, J.; Henry, A.; Wahab, Q.; Bergman, J.; Makarov, Y.; Vorob'ev, A.; Vehanen, A.; Janzén, E. High temperature CVD growth of SiC. *Mater. Sci. Eng., B* **1999**, *61–62*, 113–120.
- (61) Laskowski, R.; Blaha, P.; Gallauner, T.; Schwarz, K. Single-Layer Model of the Hexagonal Boron Nitride Nanomesh on the Rh(111) Surface. *Phys. Rev. Lett.* **2007**, *98*, 106802.
- (62) Preobrajenski, A.; Nesterov, M.; Ng, M. L.; Vinogradov, A.; Mårtensson, N. Monolayer h-BN on lattice-mismatched metal surfaces: On the formation of the nanomesh. *Chem. Phys. Lett.* **2007**, *446*, 119–123.
- (63) Liu, X.; Balla, I.; Bergeron, H.; Hersam, M. C. Point Defects and Grain Boundaries in Rotationally Commensurate MoS<sub>2</sub> on Epitaxial Graphene. *J. Phys. Chem. C* **2016**, *120*, 20798–20805.
- (64) Zhang, C.; Johnson, A.; Hsu, C.-L.; Li, L.-J.; Shih, C.-K. Direct Imaging of Band Profile in Single Layer MoS<sub>2</sub> on Graphite: Quasiparticle Energy Gap, Metallic Edge States, and Edge Band Bending. *Nano Lett.* **2014**, *14*, 2443–2447.
- (65) Bruix, A.; Miwa, J. A.; Hauptmann, N.; Wegner, D.; Ulstrup, S.; Grønberg, S. S.; Sanders, C. E.; Dendzik, M.; Grubišić Čabo, A.; Bianchi, M.; Lauritsen, J. V.; Khajetoorians, A. A.; Hammer, B.; Hofmann, P. Single-layer MoS<sub>2</sub> on Au(111): Band gap renormalization and substrate interaction. *Phys. Rev. B: Condens. Matter Mater. Phys.* **2016**, *93*, 165422.
- (66) Li, Q.; Zou, X.; Liu, M.; Sun, J.; Gao, Y.; Qi, Y.; Zhou, X.; Yakobson, B. I.; Zhang, Y.; Liu, Z. Grain Boundary Structures and Electronic Properties of Hexagonal Boron Nitride on Cu(111). *Nano Lett.* **2015**, *15*, 5804–5810.
- (67) Hwang, B.; Kwon, J.; Lee, M.; Lim, S.; Jeon, S.; Kim, S.; Ham, U.; Song, Y.; Kuk, Y. Electron-beam assisted growth of hexagonal boron-nitride layer. *Curr. Appl. Phys.* **2013**, *13*, 1365–1369.
- (68) Elias, C.; Valvin, P.; Pelini, T.; Summerfield, A.; Mellor, C. J.; Cheng, T. S.; Eaves, L.; Foxon, C. T.; Beton, P. H.; Novikov, S. V.; Gil, B.; Gil, B. Direct band-gap crossover in epitaxial monolayer boron nitride. *Nat. Commun.* **2019**, *10* (1), 2639.
- (69) Paleari, F.; Galvani, T.; Amara, H.; Ducastelle, F.; Molina-Sánchez, A.; Wirtz, L. Excitons in few-layer hexagonal boron nitride: Davydov splitting and surface localization. *2D Mater.* **2018**, *5*, 045017.
- (70) Coraux, J.; N'Diaye, A. T.; Engler, M.; Busse, C.; Wall, D.; Buckanie, N.; zu Heringdorf, F.-J. M.; van Gastel, R.; Poelsema, B.; Michely, T. Growth of graphene on Ir(111). *New J. Phys.* **2009**, *11*, 039801.
- (71) Voloshina, E. N.; Fertitta, E.; Garhofer, A.; Mittendorfer, F.; Fonin, M.; Thissen, A.; Dedkov, Y. S. Electronic structure and imaging contrast of graphene moiré on metals. *Sci. Rep.* **2013**, *3*, 1072.
- (72) Mazzoni, M. S. C.; Nunes, R. W.; Azevedo, S.; Chacham, H. Electronic structure and energetics of B<sub>x</sub>C<sub>y</sub>N<sub>z</sub> layered structures. *Phys. Rev. B: Condens. Matter Mater. Phys.* **2006**, *73*, 073108.
- (73) Yuge, K. Phase stability of boron carbon nitride in a heterographene structure: A first-principles study. *Phys. Rev. B: Condens. Matter Mater. Phys.* **2009**, *79*, 144109.
- (74) Ren, X.; Xia, S.; Zhang, Z.; Meng, X.; Yu, H.; Wu, Q.; Zhang, W.; Li, A.; Yang, H. Opening of Band Gap of Graphene with High Electronic Mobility by Codoping BN Pairs. *Chem. Res. Chin. Univ.* **2019**, *35*, 1058–1061.
- (75) N'Diaye, A. T.; Bleikamp, S.; Feibelman, P. J.; Michely, T. Two-Dimensional Ir Cluster Lattice on a Graphene Moiré on Ir(111). *Phys. Rev. Lett.* **2006**, *97*, 215501.
- (76) Balog, R.; et al. Bandgap opening in graphene induced by patterned hydrogen adsorption. *Nat. Mater.* **2010**, *9*, 315–319.
- (77) Ren, X.-Y.; Xia, S.; Li, X.-B.; Chen, N.-K.; Wang, X.-P.; Wang, D.; Chen, Z.-G.; Zhang, S.; Sun, H.-B. Non-phase-separated 2D B-C-N alloys via molecule-like carbon doping in 2D BN: atomic structures and optoelectronic properties. *Phys. Chem. Chem. Phys.* **2018**, *20*, 23106–23111.
- (78) Fan, X.; Shen, Z.; Liu, A. Q.; Kuo, J.-L. Band gap opening of graphene by doping small boron nitride domains. *Nanoscale* **2012**, *4*, 2157–2165.
- (79) Azevedo, S. Energetic stability of B-C-N monolayer. *Phys. Lett. A* **2006**, *351*, 109–112.
- (80) Tersoff, J.; Hamann, D. R. Theory and Application for the Scanning Tunneling Microscope. *Phys. Rev. Lett.* **1983**, *50*, 1998–2001.
- (81) Tersoff, J.; Hamann, D. R. Theory of the scanning tunneling microscope. *Phys. Rev. B: Condens. Matter Mater. Phys.* **1985**, *31*, 805–813.
- (82) Hämäläinen, S. K.; Boneschanscher, M. P.; Jacobse, P. H.; Swart, I.; Pussi, K.; Moritz, W.; Lahtinen, J.; Liljeroth, P.; Sainio, J. Structure and local variations of the graphene moiré on Ir(111). *Phys. Rev. B: Condens. Matter Mater. Phys.* **2013**, *88*, 201406.
- (83) Lacovig, P.; Pozzo, M.; Alfè, D.; Vilmercati, P.; Baraldi, A.; Lizzit, S. Growth of Dome-Shaped Carbon Nanolands on Ir(111): The Intermediate between Carbide Clusters and Quasi-Free-Standing Graphene. *Phys. Rev. Lett.* **2009**, *103*, 166101.
- (84) de Campos Ferreira, R. C.; de Lima, L. H.; Barreto, L.; Silva, C. C.; Landers, R.; de Siervo, A. Unraveling the Atomic Structure of Fe Intercalated under Graphene on Ir(111): A Multitechnique Approach. *Chem. Mater.* **2018**, *30*, 7201–7210.
- (85) Xu, X.; Liu, C.; Sun, Z.; Cao, T.; Zhang, Z.; Wang, E.; Liu, Z.; Liu, K. Interfacial engineering in graphene bandgap. *Chem. Soc. Rev.* **2018**, *47*, 3059–3099.
- (86) Cheng, L.; Meng, J.; Pan, X.; Lu, Y.; Zhang, X.; Gao, M.; Yin, Z.; Wang, D.; Wang, Y.; You, J.; Zhang, J.; Xie, E. Two-dimensional hexagonal boron-carbon-nitrogen atomic layers. *Nanoscale* **2019**, *11*, 10454–10462.

- (87) Ba, K.; Jiang, W.; Cheng, J.; Bao, J.; Xuan, N.; Sun, Y.; Liu, B.; Xie, A.; Wu, S.; Sun, Z. Chemical and Bandgap Engineering in Monolayer Hexagonal Boron Nitride. *Sci. Rep.* **2017**, *7*, 45584.
- (88) Chen, C.; Avila, J.; Wang, S.; Yang, R.; Zhang, G.; Asensio, M. C. Electronic structure of graphene/hexagonal boron nitride heterostructure revealed by Nano-ARPES. *Journal of Physics: Conference Series* **2017**, *864*, 012005.
- (89) Lisi, S.; et al. Observation of flat bands in twisted bilayer graphene. *Nat. Phys.* **2021**, *17*, 189.
- (90) Horcas, I.; Fernández, R.; Gómez-Rodríguez, J. M.; Colchero, J.; Gómez-Herrero, J.; Baro, A. M. WSXM: A software for scanning probe microscopy and a tool for nanotechnology. *Rev. Sci. Instrum.* **2007**, *78*, 013705.
- (91) Nečas, D.; Klapetek, P. Gwyddion: an open-source software for SPM data analysis. *Open Physics* **2012**, *10*, 181–188.
- (92) Giannozzi, P.; et al. QUANTUM ESPRESSO: a modular and open-source software project for quantum simulations of materials. *J. Phys.: Condens. Matter* **2009**, *21*, 395502.
- (93) Kresse, G.; Joubert, D. From ultrasoft pseudopotentials to the projector augmented-wave method. *Phys. Rev. B: Condens. Matter Mater. Phys.* **1999**, *59*, 1758–1775.
- (94) Perdew, J. P.; Burke, K.; Ernzerhof, M. Generalized Gradient Approximation Made Simple. *Phys. Rev. Lett.* **1996**, *77*, 3865–3868.